Chemical Science

ROYAL SOCIETY OF CHEMISTRY

EDGE ARTICLE

View Article Online
View Journal | View Issue

Cite this: *Chem. Sci.*, 2024, **15**, 5548

Improving the hydrothermal stability of Al-rich Cu-SSZ-13 zeolite *via* Pr-ion modification†

Mengyang Chen, ‡[a] Wenru Zhao, ‡[c] Yingzhen Wei,[b] Shi-Bin Ren,[a] Yuxiang Chen,[a] Donghai Mei, *[c] De-Man Han *[a] and Jihong Yu *[bd]

Received 30th November 2023
Accepted 8th March 2024

DOI: 10.1039/d3sc06422k

rsc.li/chemical-science

Al-rich (Si/Al = 4–6) Cu-SSZ-13 has been recognized as one of the potential catalysts to replace the commercial Cu-SSZ-13 (Si/Al = 10–12) towards ammonia-assisted selective catalytic reduction (NH_3-SCR). However, poor hydrothermal stability is a great obstacle for Al-rich zeolites to meet the catalytic applications containing water vapor. Herein, we demonstrate that the hydrothermal stability of Al-rich Cu-SSZ-13 can be dramatically enhanced *via* Pr-ion modification. Particularly, after high-temperature hydrothermal aging (HTA), $CuPr_{1.2}$-SSZ-13-HTA with an optimal Pr content of 1.2 wt% exhibits a T_{80} (temperature window of NO conversion above 80%) window of 225–550 °C and a T_{90} window of 250–350 °C. These values are superior to those of Cu-SSZ-13-HTA (225–450 °C for T_{80} and no T_{90} window). The results of X-ray diffraction Rietveld refinement, electron paramagnetic resonance (EPR) and spectral characterization reveal that Pr ions mainly located in the eight-membered rings (8MRs) in SSZ-13 zeolite can inhibit the generation of inactive CuO_x during hydrothermal aging. This finding is further supported by density functional theory (DFT) calculations, which suggest that the presence of Pr ions restrains the transformation from Cu^{2+} ions in 6MRs into CuO_x, resulting in enhanced hydrothermal stability. It is also noted that an excessive amount of Pr ions in Cu-SSZ-13 would result in the production of CuO_x that causes the decline of catalytic performance. The present work provides a promising strategy for creating a hydrothermally stable Cu-SSZ-13 zeolite catalyst by adding secondary metal ions.

Introduction

Currently, environmental issues, especially air pollution, have been the focus of the whole society. Nitrogen oxides (NO_x), mainly generated from vehicle exhaust emissions, have received significant attention due to their adverse impacts on human health and the environment.[1–3] Consequently, the development of effective strategies for eliminating NO_x has become crucial. Among these strategies, ammonia-mediated selective catalytic reduction (NH_3-SCR) has emerged as a highly efficient and environmentally friendly technology.[4–6] Cu ion-exchanged SSZ-13 zeolite (Cu-SSZ-13) has been successfully employed in NH_3-SCR applications for heavy-duty transportation trucks.[7–9] However, two technical challenges still remain to be solved: (1) high-temperature hydrothermal stability caused by the regeneration of the diesel particulate filter (DPF) and (2) low-temperature (≤200 °C) catalytic activity during the cold start.[2,4,10,11]

Previous studies have demonstrated that introducing secondary metal ions into Cu-SSZ-13 is an effective approach for addressing the above issues.[12–21] These secondary metal ions play various roles, including (1) regulating the distribution of Cu sites, such as $[ZCu(OH)]^+$ (Cu ions in eight-membered rings (8MRs), where Z represents a negative charge in the zeolite framework) and Z_2Cu^{2+} (Cu ions in 6MRs); (2) enhancing the hydrothermal stability of the structure by restraining the formation of inactive CuO_x; (3) creating the synergistic effect with Cu sites and (4) ion-exchanging with Brønsted acid sites (BASs) to prevent the attack of H_2O during hydrothermal aging.[12–21] For example, the presence of alkali metal ions in SSZ-13 can reduce part of Brønsted sites, which was helpful for the enhanced hydrothermal stability.[16] In addition, Co^{2+} ions as co-cations in Cu-SSZ-13 favour the generation of highly active $[ZCu(OH)]^+$, thereby improving low-temperature NH_3-SCR activity.[17] Recently, Cu–Ce-SSZ-13 was reported to show superior hydrothermal stability compared to Cu-SSZ-13.[19] Moreover, Cu-Sm-SSZ-13 was demonstrated to display higher NH_3-SCR performance relative to Cu-SSZ-13, which was because Sm ions

---

[a] *School of Pharmaceutical and Chemical Engineering, Taizhou University, Taizhou 318000, P. R. China. E-mail: hdmtzc@126.com*

[b] *State Key Laboratory of Inorganic Synthesis and Preparative Chemistry, College of Chemistry, Jilin University, Changchun, 130012, P. R. China. E-mail: jihong@jlu.edu.cn*

[c] *School of Materials Science and Engineering, Tiangong University, Tianjin 300387, China. E-mail: dhmei@tiangong.edu.cn*

[d] *International Center of Future Science, Jilin University, Changchun, 130012, P. R. China*

† Electronic supplementary information (ESI) available. See DOI: https://doi.org/10.1039/d3sc06422k

‡ These authors contributed equally.

occupying the 6MRs can regulate the characteristics of Cu sites.[20] Note that Pr ions show similar physicochemical properties to Ce ions and Sm ions, however, the effects of introducing Pr ions on the NH_3-SCR performance of Cu-SSZ-13 have been rarely investigated.

Al-rich (Si/Al = 4–6) Cu-SSZ-13 zeolite, characterized by a higher aluminium content (Si/Al = 4–6), has emerged as a potential alternative to the commercial Cu-SSZ-13 (Si/Al = 10–12).[22,23] The increased aluminium content in Al-rich SSZ-13 provides sufficient ion exchange sites for loading more Cu species. This, in turn, enhances the low-temperature NH_3-SCR activity, thus meeting the requirement under cold-start conditions.[24–26] However, excessive Cu ions are prone to aggregate to form CuO_x accompanied by dealumination and the destruction of the Al-rich Cu-SSZ-13 structure during hydrothermal aging. To overcome these challenges, a promising solution is to suppress the migration of Cu^{2+} ions during hydrothermal treatment and consequently decrease the formation of inactive CuO_x.

In this work, we demonstrated that introducing an appropriate amount of Pr ions into Al-rich Cu-SSZ-13 can significantly enhance its hydrothermal stability without affecting its catalytic activity. Various experimental characterization studies revealed that Pr ions occupied the 8MRs and the center of the CHA cage in the SSZ-13 zeolite, which inhibited the migration of Z_2Cu^{2+} ions to form CuO_x during hydrothermal aging. To gain deeper insights into the underlying mechanism for the enhanced hydrothermal stability, first principles density functional theory (DFT) calculations were performed. The results indicated that the existence of Pr ions can increase the activation barriers for Z_2Cu^{2+} transforming into inactive CuO_x species, thus enhancing the hydrothermal stability. However, an excessive amount of Pr ions in the Cu-SSZ-13 zeolite can negatively impact the high-temperature (≥450 °C) activity and hydrothermal stability of the catalyst.

Results and discussion

Structural characterization and NH_3-SCR performance

X-ray diffraction (XRD) Rietveld refinement and XRD electron density distribution were applied to investigate the locations of Pr ions in Pr-SSZ-13 with the Pr loading of 1.2 wt% (Fig. S1, Table S1† and Fig. 1a). It can be observed that Pr ions are mainly located in 8MRs as well as marginally in the CHA cage of SSZ-13 (Fig. 1b). According to the above results, Pr ions appropriately act as the "barrier" to inhibit the migration of Cu ions in 6MRs during hydrothermal aging (HTA). Therefore, the solid-state ion-exchange method was conducted to incorporate Pr ions into Cu-SSZ-13 to obtain CuPr-SSZ-13 samples with various Pr content. Cu-SSZ-13 and Pr-SSZ-13 samples were also prepared by ion-exchanging Cu and Pr ions, respectively, to serve as a comparison. According to the corresponding chemical composition studies described in Table S2,† Pr content increases from $CuPr_{0.6}$-SSZ-13 (0.6 wt%) to $CuPr_{2.4}$-SSZ-13 (2.4 wt%) with increasing Pr precursors in the synthesis system. In addition, the Si/Al ratios (~6) and Cu concentrations (~2.30 wt%) are comparable among all samples. To simulate actual aging conditions, these samples were further treated for ten hours at 800 °C in flowing air with 10 vol% H_2O, and they were denoted as Cu-SSZ-13-HTA and CuPr-SSZ-13-HTA, respectively.

The XRD patterns of SSZ-13 zeolites are displayed in Fig. S2.† Prior to hydrothermal aging, each sample exhibits characteristic diffraction peaks of SSZ-13 (Fig. S2a†). The intensities of diffraction peaks decrease from Cu-SSZ-13 to $CuPr_{2.4}$-SSZ-13 as the Pr content increases, which is due to the introduction of Pr ions that absorb part of X-rays. After hydrothermal aging (Fig. S2b†), the diffraction peaks of SSZ-13 of each sample remain intact. $CuPr_{1.2}$-SSZ-13-HTA exhibits higher peak intensity than Cu-SSZ-13-HTA and $CuPr_{2.4}$-SSZ-13-HTA. This observation suggests that incorporating an appropriate amount of Pr ions can enhance the hydrothermal stability of Cu-SSZ-13. Excessive Pr ions can have a detrimental effect on the zeolite structure to some extent, as indicated by the lower peak intensity in $CuPr_{2.4}$-SSZ-13-HTA.

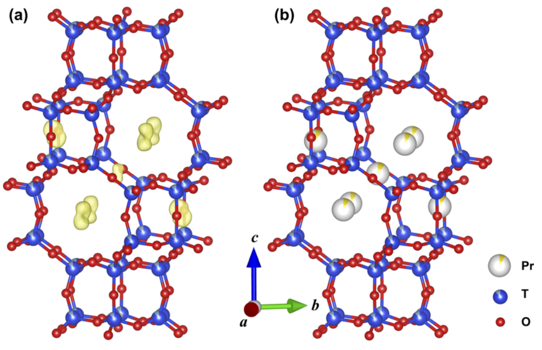

Fig. 1 Difference electron density distribution (a) and locations of Pr ions (b) in Pr-SSZ-13 viewed along the [100] direction. Data from Rietveld refinement against PXRD.

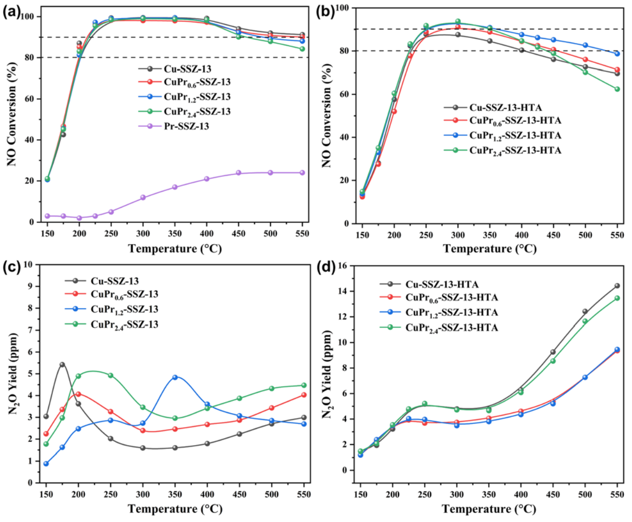

Fig. 2 (a) and (b) NO conversion and (c) and (d) N_2O yield as a function of temperature for SSZ-13 samples before and after hydrothermal aging. Standard SCR conditions: 500 ppm NO, 500 ppm NH_3, 5% O_2, and 5% H_2O, balanced with N_2 at a GHSV of 200 000 h^{-1}.

Fig. 2a displays the NH_3-SCR performance of fresh SSZ-13 zeolites. It is noteworthy that Pr-SSZ-13 exhibits extremely low activity over the whole temperature range, whose observed NO conversion only reaches 20% at 450–550 °C. In contrast, Cu-SSZ-13 shows excellent catalytic activity, achieving a temperature window of NO conversion above 90% (T_{90}) at 225–550 °C. When Pr ions are introduced into Cu-SSZ-13, $CuPr_{0.6}$-SSZ-13 and $CuPr_{1.2}$-SSZ-13 exhibit similar activity to Cu-SSZ-13, while $CuPr_{2.4}$-SSZ-13 shows slightly lower NO conversion than Cu-SSZ-13 at the temperatures above 450 °C. After hydrothermal aging, the catalytic activities of all samples decline compared to their fresh counterparts (Fig. 2b). Cu-SSZ-13-HTA displays a T_{80} window of 225–400 °C without T_{90} window. $CuPr_{0.6}$-SSZ-13-HTA and $CuPr_{1.2}$-SSZ-13-HTA exhibit superior catalytic activity to Cu-SSZ-13-HTA at 300–550 °C. Particularly, $CuPr_{1.2}$-SSZ-13-HTA exhibits a T_{80} window of 225–550 °C and T_{90} window of 250–350 °C. Regarding $CuPr_{2.4}$-SSZ-13-HTA, although it exhibits higher activity than Cu-SSZ-13-HTA between 250 and 400 °C, its NO conversion starts to decline as the temperature further increases, which is probably because excess Pr ions can block the channels of zeolite and obscure part of active Cu sites. Additionally, the results of N_2O production shown in Fig. 2c indicate that the N_2O yield of each fresh sample is less than 6 ppm throughout the whole temperature range. Noticeably, the N_2O yields of all aged samples increase at high temperatures (>300 °C) (Fig. 2d), which is due to the formation of CuO_x during hydrothermal aging.[6] Cu-SSZ-13-HTA and $CuPr_{2.4}$-SSZ-13-HTA exhibit higher N_2O yields than $CuPr_{0.6}$-SSZ-13-HTA and $CuPr_{1.2}$-SSZ-13-HTA above 250 °C, indicating their inferior N_2 selectivity.

The functions of Pr ions

It is acknowledged that electron paramagnetic resonance (EPR) is a valuable technique for investigating the relative active Cu content in Cu-SSZ-13 zeolites. In Fig. 3a, the peak at approximately 3250 G is assigned to the isolated Cu active sites.[27,28] Fresh Cu-SSZ-13 zeolite possesses a completed hyperfine structure corresponding to Cu^{2+} ions. However the hyperfine structure in Cu-SSZ-13-HTA suffers from serious destruction after hydrothermal aging, suggesting the aggregation of Cu^{2+} ions. Meanwhile, the intensity of the peak at 3250 G in Cu-SSZ-13-HTA decreases sharply compared to that of fresh Cu-SSZ-13. This decrease can be attributed to the migration and aggregation of Cu sites forming EPR-silent CuO_x during hydrothermal treatment. Similarly, $CuPr_{1.2}$-SSZ-13-HTA displays weaker intensity of the peak at 3250 G and destructive hyperfine structure compared to fresh $CuPr_{1.2}$-SSZ-13 (Fig. 3b). Notably, the relative peak intensity difference between $CuPr_{1.2}$-SSZ-13 and $CuPr_{1.2}$-SSZ-13-HTA is smaller than that between Cu-SSZ-13 and Cu-SSZ-13-HTA. This suggests that the incorporation of Pr ions can suppress the formation of CuO_x during hydrothermal treatment, allowing for the preservation of more Cu active sites in $CuPr_{1.2}$-SSZ-13-HTA.

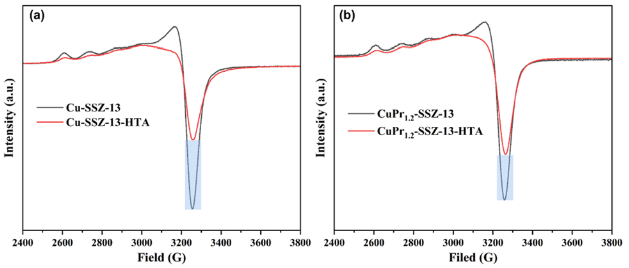

Fig. 3 EPR spectra of (a) Cu-SSZ-13 and (b) $CuPr_{1.2}$-SSZ-13 before and after hydrothermal aging.

The nitrogen adsorption–desorption isotherms of fresh SSZ-13 zeolites, as depicted in Fig. S3,† display the type I isotherms, indicating the microporosity of both samples. The initial BET area and micropore volume of Cu-SSZ-13 are 512 $m^2\ g^{-1}$ and 0.24 $cm^3\ g^{-1}$, respectively (Table S2†). However, the BET area and micropore volume of CuPr-SSZ-13 zeolites gradually decrease with increasing Pr ion content. Specifically, $CuPr_{2.4}$-SSZ-13 shows a BET area of 409 $m^2\ g^{-1}$ and a micropore volume of 0.19 $cm^3\ g^{-1}$. This reduction can be attributed to the occupation of the SSZ-13 zeolite channels by the introduced Pr ions.

Scanning electron microscope (SEM) images of SSZ-13 zeolites, as displayed in Fig. S4,† indicate their similar morphologies with cubic crystals ranging in size from 2 to 5 μm. This suggests that the introduction of Pr ions does not damage the morphology of SSZ-13. In addition, metal ion aggregates are not observed on the crystal surface of $CuPr_{1.2}$-SSZ-13, suggesting that Pr species mainly exist in the form of ions in the channel of SSZ-13. Moreover, transmission electron microscope (TEM) analyses (Fig. S5†) show that black dots corresponding to CuO_x appear in the aged samples. Note that compared to $CuPr_{1.2}$-SSZ-13-HTA, more black dots with larger sizes appear in Cu-SSZ-13-HTA, suggesting a higher amount of CuO_x in Cu-SSZ-13-HTA. Elemental mapping characterization was carried out to investigate the metal dispersion of representative $CuPr_{1.2}$-SSZ-13 before and after hydrothermal aging. As shown in Fig. S6,† all elements in $CuPr_{1.2}$-SSZ-13 and $CuPr_{1.2}$-SSZ-13-HTA are well-dispersed, indicating that the incorporation of Pr ions does not result in the aggregation of Cu ions and maintains the good dispersion of bimetallic ions in the zeolites even after hydrothermal treatment.

^{27}Al magic angle spin nuclear magnetic resonance (MAS NMR) measurement as a semi-quantitative tool was used to estimate the Al content in the samples before and after the hydrothermal aging treatment. As shown in Fig. S7,† the tetracoordinated framework Al (Al_F) is responsible for the peak at 58 ppm, whilst the pentacoordinated and hexacoordinated extraframework Al (Al_{EF}) are responsible for the peaks at 33 and 0.4 ppm, respectively.23,29 Taking the framework Al (Al_F) signal area of each fresh sample as unity, the amounts of Al_F in the aged samples are normalized. The $CuPr_{1.2}$-SSZ-HTA sample displays more Al_F (0.77) than the Cu-SSZ-13-HTA sample (0.70), which indicates that more pronounced degradation occurs in Cu-SSZ-13-HTA without the introduction of Pr ions. Note that the intensities of the signal at 0.4 ppm in aged samples become stronger due to dealumination during hydrothermal aging. However, it is also observed that this signal remains almost unchanged in each aged sample, which can be largely attributed to that either the portion of Al species are in the close vicinity of paramagnetic Cu^{2+} ions to suppress the Al NMR resonances or the ^{27}Al NMR experiment cannot detect the detached Al species in highly distorted sites in the zeolite.[27] The findings of fitting ^{27}Al MAS NMR spectra, shown in Fig. S8 and Table S3,† further illustrate the changes in Al distribution in the aged zeolites. In both hydrothermally aged zeolites, it is seen that framework Al is predominantly accompanied by the existence of extra-framework Al. $CuPr_{1.2}$-SSZ-13-HTA displays a higher proportion of framework Al and a lower proportion of extra-framework Al compared to Cu-SSZ-13-HTA, which further confirms that introducing Pr ions can enhance the hydrothermal stability of Cu-SSZ-13.

Cu 2p X-ray photoelectron spectroscopy (XPS) was conducted to examine the surface Cu species of SSZ-13 zeolites. As illustrated in Fig. S9,† the intensities of the Cu $2p_{1/2}$ peak corresponding to Cu^{2+} in aged zeolites become weaker compared to that in fresh counterparts, suggesting the formation of CuO_x.[15,18,30] In addition, each Cu $2p_{3/2}$ peak can be divided into two peaks with the CuO-attributed peak at 934.1 eV and the Cu^{2+}-attributed peak at 935.7 eV. Before hydrothermal aging, each sample shows higher intensity of the Cu^{2+} peak and lower intensity of the CuO peak. However, after hydrothermal treatment, the intensity of the Cu^{2+} peak becomes weaker and lower than that of the CuO peak in each aged sample, indicating the production of CuO_x during hydrothermal aging. Interestingly, the intensity of the Cu^{2+} peak is similar to that of the CuO peak in $CuPr_{1.2}$-SSZ-13-HTA while the intensity of the CuO peak is higher than that of the Cu^{2+} peak in Cu-SSZ-13-HTA. This difference between Cu-SSZ-13-HTA and $CuPr_{1.2}$-SSZ-13-HTA indicates that the role of Pr ions is to prevent CuO_x from forming during hydrothermal aging, which allows $CuPr_{1.2}$-SSZ-13-HTA to retain more Cu^{2+} sites after hydrothermal treatment.

Temperature-programmed desorption of ammonia (NH_3-TPD) experiments were carried out to investigate the acidity of SSZ-13 zeolites. Three peaks are visible in the fresh samples (Fig. S10†). NH_3 molecules adsorbed on weak acid sites give rise to the first peak at 180 °C, while NH_3 molecules adsorbed on Lewis acid sites (mostly Cu^{2+} sites) give rise to the middle peak at 340 °C.[31–33] NH_3 molecules adsorbed at BASs are responsible for the peak observed above 450 °C. Note that the total acid concentration of $CuPr_{1.2}$-SSZ-13 is slightly higher than that of Cu-SSZ-13, primarily due to NH_3 molecules adsorbed on Pr ion sites. After hydrothermal aging, the amount of acid concentration in aged samples decreases compared to that in their fresh counterparts, suggesting that zeolites suffer from dealumination and the damage of the structure during hydrothermal aging. $CuPr_{1.2}$-SSZ-13-HTA has a higher acid concentration than Cu-SSZ-13-HTA, indicating that the presence of Pr ions can improve the hydrothermal stability of SSZ-13 zeolites.

The distributions of Cu species in SSZ-13 zeolites were investigated using temperature-programmed reduction of hydrogen (H_2-TPR) experiments. As illustrated in Fig. S11,† the reduction of $[ZCu(OH)]^+$ is responsible for the first peak at 210 °C, while the reduction of CuO_x and Z_2Cu^{2+} is responsible for the peaks at 302 and 386 °C, respectively.[34–37] Additionally, there is a peak above 500 °C associated with the reduction of Cu^+ species. $[ZCu(OH)]^+$ and Z_2Cu^{2+} are predominant in fresh SSZ-13 samples accompanied by a small amount of CuO_x. After high-temperature hydrothermal treatment, the intensities of the peak at 210 °C in both aged zeolites significantly decrease with the increasing intensities of the peaks at 302 and 386 °C compared to their fresh counterparts, which is because of the transformations of $[ZCu(OH)]^+$ (to Z_2Cu^{2+} or CuO_x) and Z_2Cu^{2+} (to CuO_x) during hydrothermal aging. Importantly, when comparing $CuPr_{1.2}$-SSZ-13-HTA with Cu-SSZ-13-HTA, the former exhibits a higher peak intensity at 386 °C and a lower peak intensity at 302 °C. This suggests that $CuPr_{1.2}$-SSZ-13-HTA possesses a higher concentration of Z_2Cu^{2+} and a lower concentration of CuO_x. Furthermore, $CuPr_{1.2}$-SSZ-13-HTA shows a stronger peak at 210 °C compared to Cu-SSZ-13-HTA, indicating a higher content of $[ZCu(OH)]^+$ species. These findings provide evidence for the higher hydrothermal stability of $CuPr_{1.2}$-SSZ-13 zeolite.

To gain further insights into the role of Pr ions, ultraviolet–visible diffuse reflectance (UV–vis DRS) spectra were recorded to investigate the changes of Cu species in SSZ-13 zeolites. The spectra of fresh Cu-SSZ-13 and fresh $CuPr_{1.2}$-SSZ-13, as depicted in Fig. 4, exhibit similar characteristics with two distinct absorption bands visible in both samples. The band observed at 210 nm is assigned to the charge transfer between the framework oxygen and Cu^{2+} ions, while the band in the range of 600–800 nm arises from the electron d–d transitions of Cu^{2+} ions in octahedral Cu species.[38–40] After hydrothermal aging, a new peak at 250 nm related to CuO_x appears in the spectra of aged zeolites. Note that $CuPr_{1.2}$-SSZ-13-HTA exhibits a higher intensity difference between the peak at 210 nm and the peak at 250 nm compared to Cu-SSZ-13-HTA. This observation indicates that more Cu^{2+} ions are preserved and less CuO_x species are generated in $CuPr_{1.2}$-SSZ-13-HTA. Thus, Pr ions have the capacity of suppressing the formation of CuO_x species during the hydrothermal aging process. These findings align with the other characterization results discussed above, further supporting the role of Pr ions in improving the hydrothermal stability of Al-rich Cu-SSZ-13.

In brief, the hydrothermal stability of aged zeolites depends on its Z_2Cu^{2+} and CuO_x content. Based on the characterization analysis of Cu species, it can be concluded that $CuPr_{1.2}$-SSZ-13-HTA possesses more Z_2Cu^{2+} and less CuO_x showing superior hydrothermal stability, while Cu-SSZ-13-HTA possesses less Z_2Cu^{2+} and more CuO_x displaying inferior hydrothermal stability.

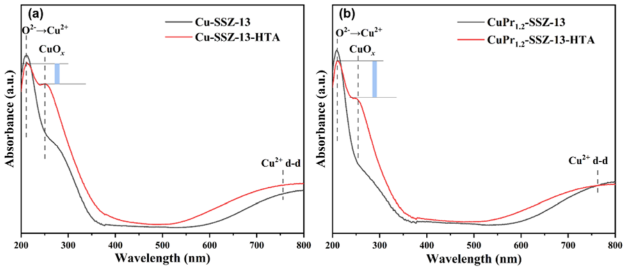

Fig. 4 UV-Vis DRS spectra of (a) Cu-SSZ-13 and Cu-SSZ-13-HTA and (b) $CuPr_{1.2}$-SSZ-13 and $CuPr_{1.2}$-SSZ-13-HTA.

DFT calculations

To understand the key role of adding the secondary Pr ions in the enhanced hydrothermal stability, DFT calculations were first employed to explore the possible locations and types of trivalent Pr ions in Cu-SSZ-13 zeolite. As indicated by our previous studies,[20,21] $[Z_2Pr^{3+}(OH)]^{2+}$ and $[ZPr^{3+}(OH)_2]^+$ are the most likely types of trivalent Pr cations in the zeolites, which might be located in either the 8MR or the CHA cage of Cu-SSZ-13 zeolite. The relative thermodynamic stabilities of $[Z_2Pr^{3+}(OH)]^{2+}$ and $[ZPr^{3+}(OH)_2]^+$ at both locations are examined using the following equations that represent the ion-exchange processes between the protons at BAS sites and the $[Z_2Pr^{3+}(OH)]^{2+}$ and $[ZPr^{3+}(OH)_2]^+$ ions. The corresponding structures are provided in Fig. S12.†

$$Pr(OH)_3 + 2H^+Z_2(8MR)/Cu\text{-}SSZ\text{-}13 \rightarrow [Z_2Pr^{3+}(OH)]^{2+}(8MR)/Cu\text{-}SSZ\text{-}13 + 2H_2O \quad (1)$$

$$Pr(OH)_3 + 2H^+Z_2(CHA\text{-}cage)/Cu\text{-}SSZ\text{-}13 \rightarrow [Z_2Pr^{3+}(OH)]^{2+}(CHA\text{-}cage)/Cu\text{-}SSZ\text{-}13 + 2H_2O \quad (2)$$

$$Pr(OH)_3 + H^+Z(8MR)/Cu\text{-}SSZ\text{-}13 \rightarrow [ZPr^{3+}(OH)_2]^+(8MR)/Cu\text{-}SSZ\text{-}13 + H_2O \quad (3)$$

$$Pr(OH)_3 + H^+Z(CHA\text{-}cage)/Cu\text{-}SSZ\text{-}13 \rightarrow [ZPr^{3+}(OH)_2]^+(CHA\text{-}cage)/Cu\text{-}SSZ\text{-}13 + H_2O \quad (4)$$

Our DFT calculated energy changes for the above ion-exchange processes are −131.9, −182.0, −278.1 and −247.8 kJ mol^{-1}, respectively, suggesting the $[ZPr^{3+}(OH)_2]^+$ ion in the 8MR is the most thermodynamically preferred location.

DFT calculations were then performed to investigate the transformation process of a Z_2Cu^{2+} ion in the 6MR forming a free $Cu(OH)_2$ molecule inside the zeolite pore in the presence/absence of the $[ZPr^{3+}(OH)_2]^+$ ion in the 8MR in the vicinity under hydrothermal conditions ($T = 1023$ K), *i.e.*, a two-step process is involved:

$$Z_2Cu^{2+} + H_2O \rightarrow ZH^+ + [ZCu^{2+}(OH)]^+ \quad (5)$$

$$[ZCu^{2+}(OH)]^+ + H_2O \rightarrow Z_2\text{-}2H^+ + Cu(OH)_2 \quad (6)$$

It has been found that, in the presence of $[ZPr^{3+}(OH)_2]^+$ in the 8MR, the calculated Gibbs free energies of activation for the first and second steps of the transformation process are 181.3 and 210.5 kJ mol^{-1}, respectively. These energies are significantly higher than the corresponding barriers of 108.2 and 113.5 kJ mol^{-1} observed in the absence of $[ZPr^{3+}(OH)_2]^+$ in the 8MR (Fig. 5). Clearly, the hydrothermal stability of Cu-SSZ-13 is enhanced with the presence of secondary Pr ions, which agrees well with our experimental observation.

According to previous reports,[21,41] the added secondary La and Ce ions are located in 8MRs in SSZ-13 zeolites. And La ions are demonstrated to promote the hydrothermal stability of SSZ-13 *via* inhibiting the transformation of Z_2Cu^{2+} to CuO_x during hydrothermal aging. To explore this generality that secondary cations occupying the 8MRs of SSZ-13 can enhance its hydrothermal stability, both experiments and DFT calculations for adding Ce into Cu-SSZ-13 zeolites (CuCe-SSZ-13, 0.5 wt% Ce loading) are carried out. As shown in Fig. S13,† CuCe-SSZ-13-HTA exhibits superior catalytic activity to Cu-SSZ-13-HTA, suggesting its higher hydrothermal stability with the addition of Ce ions. Moreover, the results of DFT calculations shown in Fig. S14† also confirm that a higher hydrolysis barrier for the Z_2Cu^{2+} ion in the 6MR is needed (180.3 and 139.8 kJ mol^{-1}, respectively, for the first and second steps of the Z_2Cu^{2+} to $Cu(OH)_2$ process), contributing to higher hydrothermal stability of CuCe-SSZ-13 zeolite.

In general, we found, in the present study, that the introduced Pr ions can occupy the 8MRs of Cu-SSZ-13 and subsequently inhibit the migration and aggregation of Z_2Cu^{2+} in 6MRs to form inactive CuO_x during hydrothermal aging. As a result, the hydrothermal stability of Cu-SSZ-13 zeolite is enhanced. We also note that the NH_3-SCR performances of Cu-

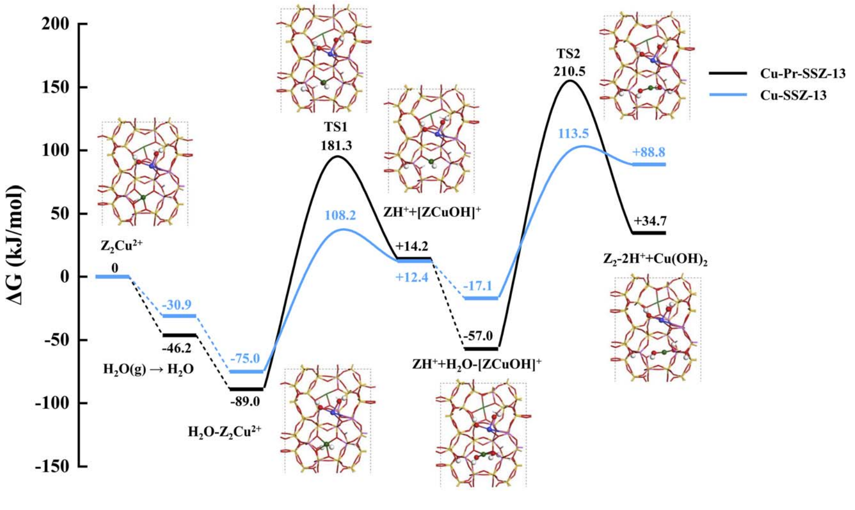

Fig. 5 DFT calculated free energy profiles for the transformation of Z_2Cu^{2+} ions in the 6MR in the absence/presence of $[ZPr^{3+}(OH)_2]^+$ in the 8MR under the hydrothermal conditions ($T = 1023$ K). The Si, O, Al, Cu, H, and Pr atoms are colored in yellow, red, magenta, blue, white and green, respectively.

SSZ-13 zeolites have been enhanced by adding secondary metal ions. For example, the stability and activity of $[ZCu(OH)]^+$ can be enhanced to promote the low-temperature activity and hydrothermal stability of zeolites by the introduction of Sm, Y, Co and Nb ions that are located in 6MRs of SSZ-13.[17,18,20,42] However La and Ce ions occupying 8MRs of SSZ-13 can improve the stability of Z_2Cu^{2+} to enhance the hydrothermal stability of zeolites.[21,41] In consequence, the roles of secondary ions largely depend upon their locations in Cu-SSZ-13 zeolites.

Conclusions

In conclusion, the present work demonstrated that loading an appropriate amount of Pr ions into Al-rich Cu-SSZ-13 catalysts can significantly enhance their resistance to hydrothermal degradation. Specifically, $CuPr_{1.2}$-SSZ-13-HTA with an optimal Pr content of 1.2 wt% exhibits wider T_{80} and T_{90} windows compared to Cu-SSZ-13-HTA after undergoing hydrothermal treatment. The introduced Pr ions are mainly located in the 8MRs of SSZ-13 zeolite, resulting in a significant increase in the activation energy for Z_2Cu^{2+} transforming into CuO_x. This in turn effectively inhibits the migration and aggregation of Z_2Cu^{2+} during hydrothermal aging, thereby improving the hydrothermal stability of Al-rich Cu-SSZ-13. However, it is important to note that an excessive amount of Pr ions in SSZ-13 can lead to the blocking of zeolite channels and the obscuring of active Cu sites, which negatively impacts catalytic activity and hydrothermal stability. This research clearly elucidates the roles of secondary Pr ions and provides a method for preparing Cu-SSZ-13 catalysts with high performance and enhanced hydrothermal stability in NH_3-SCR applications.

Author contributions

D. M., D.-M. H. and J. Y. designed and supervised the project; M. C. performed the experiments; Y. W. conducted the catalytic experiments; S.-B. R. and Y. C. checked the data; W. Z. conducted the theoretical calculation; M. C. and W. Z. wrote the first draft; D. M. and J. Y. critically revised the manuscript.

Conflicts of interest

There are no conflicts to declare.

Acknowledgements

We thank the National Natural Science Foundation of China (Nos. 21976129, 22301209, 22288101, 21920102005 and 21835002), the National Key Research and Development Program of China (Nos. 2021YFA1501202 and 2022YFA1503600), the 111 Project (B17020), the Zhejiang Province Science Technology Planning Project (No. 2021C03023) and the Zhejiang Provincial Natural Science Foundation of China (Nos. LQ20B010004). The Analytical Instrumentation Center (SPSTAIC10112914) XRD Laboratory in SPST of ShanghaiTech University is acknowledged for its help in powder XRD.

Notes and references

1 Y. Li and J. Yu, *Nat. Rev. Mater.*, 2021, **6**, 1156–1174.
2 L. Han, S. Cai, M. Gao, J.-Y. Hasegawa, P. Wang, J. Zhang, L. Shi and D. Zhang, *Chem. Rev.*, 2019, **119**, 10916–10976.
3 Q. Lin, C. Lin, J. Liu, S. Liu, H. Xu, Y. Chen and Y. Dan, *Chem. Res. Chin. Univ.*, 2020, **36**, 1249–1254.
4 Y. Shan, J. Du, Y. Zhang, W. Shan, X. Shi, Y. Yu, R. Zhang, X. Meng, F.-S. Xiao and H. He, *Natl. Sci. Rev.*, 2021, **8**, nwab010.
5 Q. Sun, N. Wang and J. Yu, *Adv. Mater.*, 2021, **33**, 2104442.
6 Y. Bai, D. Hao, Y. Wei, J. Han, D. Li, M. Chen and J. Yu, *Mater. Chem. Front.*, 2024, DOI: 10.1039/d3qm00813d.
7 M. Chen, J. Bi, C. Liu and S.-B. Ren, *Mater. Lett.*, 2023, **349**, 134872.
8 A. M. Beale, F. Gao, I. Lezcano-Gonzalez, C. H. Peden and J. Szanyi, *Chem. Soc. Rev.*, 2015, **44**, 7371–7405.
9 Y. Wei, S. Wang, M. Chen, J. Han, G. Yang, Q. Wang, J. Di, H. Li, W. Wu and J. Yu, *Adv. Mater.*, 2023, 202302912.
10 R. Simancas, A. Chokkalingam, S. P. Elangovan, Z. Liu, T. Sano, K. Iyoki, T. Wakihara and T. Okubo, *Chem. Sci.*, 2021, **12**, 7677–7695.
11 Y. Zhang, H. Zhu, T. Zhang, J. Li, J. Chen, Y. Peng and J. Li, *Environ. Sci. Technol.*, 2022, **56**, 1917–1926.
12 C. Paolucci, I. Khurana, A. A. Parekh, S. Li, A. J. Shih, H. Li, J. R. Di Iorio, J. D. Albarracin-Caballero, A. Yezerets, J. T. Miller, W. N. Delgass, F. H. Ribeiro, W. F. Schneider and R. Gounder, *Science*, 2017, **357**, 898–903.
13 Y. Wang, X. Shi, Y. Shan, J. Du, K. Liu and H. He, *Ind. Eng. Chem. Res.*, 2020, **59**, 6416–6423.
14 Z. Zhao, R. Yu, C. Shi, H. Gies, F. Xiao, D. De Vos, T. Yokoi, X. Bao, U. Kolb, M. Feyen, R. McGuire, S. Maurer, A. Moini, U. Mueller and W. Zhang, *Catal. Sci. Technol.*, 2019, **9**, 241–251.
15 M. Chen, Y. Wei, J. Han, W. Yan and J. Yu, *Mater. Chem. Front.*, 2021, **5**, 7787–7795.
16 F. Gao, Y. Wang, N. M. Washton, M. Kollár, J. Szanyi and C. H. F. Peden, *ACS Catal.*, 2015, **5**, 6780–6791.
17 H. Lee, I. Song, S. W. Jeon and D. H. Kim, *Catal. Sci. Technol.*, 2021, **11**, 4838–4848.
18 J. Wang, J. Liu, X. Tang, C. Xing and T. Jin, *Chem. Eng. J.*, 2021, **418**, 129433.
19 T. Usui, Z. Liu, S. Ibe, J. Zhu, C. Anand, H. Igarashi, N. Onaya, Y. Sasaki, Y. Shiramata, T. Kusamoto and T. Wakihara, *ACS Catal.*, 2018, **8**, 9165–9173.
20 M. Chen, J. Li, W. Xue, S. Wang, J. Han, Y. Wei, D. Mei, Y. Li and J. Yu, *J. Am. Chem. Soc.*, 2022, **144**, 12816–12824.
21 M. Chen, W. Zhao, Y. Wei, J. Han, J. Li, C. Sun, D. Mei and J. Yu, *Nano Res.*, 2023, **16**, 12126–12133.
22 J. Luo, F. Gao, K. Kamasamudram, N. Currier, C. H. F. Peden and A. Yezerets, *J. Catal.*, 2017, **348**, 291–299.
23 J. Luo, D. Wang, A. Kumar, J. Li, K. Kamasamudram, N. Currier and A. Yezerets, *Catal. Today*, 2016, **267**, 3–9.
24 Y. Shan, J. Du, Y. Yu, W. Shan, X. Shi and H. He, *Appl. Catal., B*, 2020, **266**, 118655.

25 Y. Shan, W. Shan, X. Shi, J. Du, Y. Yu and H. He, *Appl. Catal., B*, 2020, **264**, 118511.

26 S. H. Krishna, A. Goswami, Y. Wang, C. B. Jones, D. P. Dean, J. T. Miller, W. F. Schneider and R. Gounder, *Nat. Catal.*, 2023, **6**, 276–285.

27 J. Song, Y. Wang, E. D. Walter, N. M. Washton, D. Mei, L. Kovarik, M. H. Engelhard, S. Prodinger, Y. Wang, C. H. F. Peden and F. Gao, *ACS Catal.*, 2017, **7**, 8214–8227.

28 Y. Zhang, Y. Peng, J. Li, K. Groden, J.-S. McEwen, E. D. Walter, Y. Chen, Y. Wang and F. Gao, *ACS Catal.*, 2020, **10**, 9410–9419.

29 W. Wang, J. Xu and F. Deng, *Natl. Sci. Rev.*, 2022, **9**, nwac155.

30 S. Han, J. Cheng, C. Zheng, Q. Ye, S. Cheng, T. Kang and H. Dai, *Appl. Surf. Sci.*, 2017, **419**, 382–392.

31 T. Zhang, J. Li, J. Liu, D. Wang, Z. Zhao, K. Cheng and J. Li, *AIChE J.*, 2015, **61**, 3825–3837.

32 G. V. A. Martins, G. Berlier, C. Bisio, S. Coluccia, H. O. Pastore and L. Marchese, *J. Phys. Chem. C*, 2008, **112**, 7193–7200.

33 M. Chen, Q. Sun, G. Yang, X. Chen, Q. Zhang, Y. Zhang, X. Yang and J. Yu, *ChemCatChem*, 2019, **11**, 3865–3870.

34 J. Xue, X. Wang, G. Qi, J. Wang, M. Shen and W. Li, *J. Catal.*, 2013, **297**, 56–64.

35 Y. Jangjou, Q. Do, Y. Gu, L.-G. Lim, H. Sun, D. Wang, A. Kumar, J. Li, L. C. Grabow and W. S. Epling, *ACS Catal.*, 2018, **8**, 1325–1337.

36 T. Zhang, F. Qiu and J. Li, *Appl. Catal., B*, 2016, **195**, 48–58.

37 J. H. Kwak, H. Y. Zhu, J. H. Lee, C. H. F. Peden and J. Szanyi, *Chem. Commun.*, 2012, **48**, 4758–4760.

38 I. Lezcano-Gonzalez, U. Deka, H. E. van der Bij, P. Paalanen, B. Arstad, B. M. Weckhuysen and A. M. Beale, *Appl. Catal., B*, 2014, **154–155**, 339–349.

39 C. Fan, Z. Chen, L. Pang, S. Ming, C. Dong, K. Brou Albert, P. Liu, J. Wang, D. Zhu, H. Chen and T. Li, *Chem. Eng. J.*, 2018, **334**, 344–354.

40 Y. Wei, M. Chen, X. Ren, Q. Wang, J. Han, W. Wu, X. Yang, S. Wang and J. Yu, *CCS Chem.*, 2022, **4**, 1708–1719.

41 X. Wang, T. Li, C. Wang, Q. Cui, T. Wang, X. Bao and Y. Yue, *Sep. Purif. Technol.*, 2024, **331**, 125638.

42 N. Kang, Y. Wang, Z. Chen, X. Tang, Y. Wang, Z. Ding, C. Zhang, S. Dai, C. V. Singh, P. Xie and M. Yan, *Chem. Eng. J.*, 2023, **475**, 146114.